Inorganic Chemistry

Article

pubs.acs.org/IC

Insights into the Effect of Iron and Cobalt Doping on the Structure of Nanosized ZnO

Gabriele Giuli,*[†] Angela Trapananti,[‡] Franziska Mueller,[§,⊥,∥] Dominic Bresser,[§,⊥] Francesco d'Acapito,[‡] and Stefano Passerini[§,⊥]

[†]School of Science and Technology, Geology Division, Camerino University, 62032 Camerino, Italy
[‡]CNR-Istituto Officina dei Materiali (IOM)-OGG, c/o ESRF-71, Avenue des Martyrs, 38043 Grenoble, France
[§]Helmholtz Institute Ulm (HIU), Helmholtzstraße 11, 89081 Ulm, Germany
[⊥]Karlsruhe Institute of Technology (KIT), P.O. Box 3640, 76021 Karlsruhe, Germany
[∥]Institute of Physical Chemistry, University of Muenster, Corrensstraße 28/30, 48149 Muenster, Germany

Supporting Information

ABSTRACT: Here we report an in-depth structural characterization of transition metal-doped zinc oxide nanoparticles that have recently been used as anode materials for Li-ion batteries. Structural refinement of powder X-ray diffraction (XRD) data allowed the determination of small though reproducible changes in the unit cell dimensions of four ZnO samples (wurtzite structure) prepared with different dopants or different synthesis conditions. Moreover, large variations of the full width at half-maximum of the XRD reflections indicate that the crystallinity of the samples decreases in the order ZnO, $Zn_{0.9}Co_{0.1}O$, $Zn_{0.9}Fe_{0.1}O/C$, and $Zn_{0.9}Fe_{0.1}O$ (the crystallite sizes as determined by Williamson−Hall plots are 42, 29, 15, and 13 nm, respectively). X-ray absorption spectroscopy data indicate that Co is divalent, whereas Fe is purely trivalent in $Zn_{0.9}Fe_{0.1}O$ and 95% trivalent ($Fe^{3+}/(Fe^{3+} + Fe^{2+})$ ratio = 0.95) in $Zn_{0.9}Fe_{0.1}O/C$. The aliovalent substitution of Fe^{3+} for Zn^{2+} implies the formation of local defects around Fe^{3+} such as cationic vacancies or interstitial oxygen for charge balance. The EXAFS (extended X-ray absorption fine structure) data, besides providing local Fe−O and Co−O bond distances, are consistent with a large amount of charge-compensating defects. The Co-doped sample displays similar EXAFS features to those of pure ZnO, suggesting the absence of a large concentration of defects as found in the Fe-doped samples. These results are of substantial importance for understanding and elucidating the modified electrochemical lithiation mechanism by introducing transition metal dopants into the ZnO structure for the application as lithium-ion anode material.

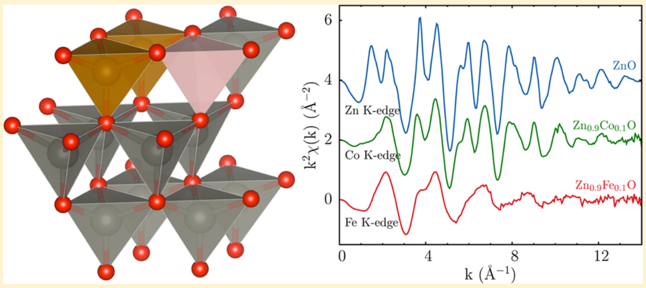

■ INTRODUCTION

In view of the use of Li-ion batteries for the aim of energy storage, alternative anode materials offering enhanced energy and power densities and/or safety are highly desirable. This is particularly true considering the use of element cathodes such as sulfur or oxygen, providing specific capacities significantly exceeding the theoretical capacity of graphite,[1,2] still the state-of-the-art anode material. Accordingly, alternative lithium-ion storage mechanisms are required, passing the intrinsic capacity limitation of insertion materials and offering substantially higher specific capacities. For this reason, basically two different classes of materials were studied in recent years: elements being able to electrochemically alloy with lithium such as tin or silicon,[3] and transition metal oxides such as cobalt oxide, which reversibly forms Li_2O and metallic cobalt if subjected to sufficiently low potentials in the presence of lithium.[4] Rather recently, moreover, a new class of materials was studied beneficially combining these two approaches, showing further advances with respect to the achievable theoretical specific capacities and rate capabilities.[5−15] Considering its nontoxicity, environmental friendliness, abundance, specific capacity exceeding 1000 mAh g^{-1}, and superior high-rate performance, carbon-coated $ZnFe_2O_4$ nanoparticles turned out to be a highly promising alternative anode material, particularly for high-power lithium-ion batteries.[12,13,15] In order to increase the energy density of such hybrid alloying/conversion materials, some of us reported very recently transition metal-doped zinc oxide as a new lithium-ion anode material, having a general chemical formula of $Zn_{0.9}TM_{0.1}O$ (TM = Fe or Co), a class of materials that has recently attracted significant interest in the field of spintronics.[16,17] These materials provide an increased contribution of the alloying reaction to the overall lithium storage mechanism, resulting in a lower operational potential and hence an enhanced energy density when exploited in a lithium-ion full-cell.[14] Initial morphological and structural

Received: March 2, 2015
Published: September 16, 2015

ACS Publications

DOI: 10.1021/acs.inorgchem.5b00493

studies revealed that the doped zinc oxide samples are phase pure, indicating that the dopant was successfully introduced into the wurtzite lattice. However, the dopant appeared to have an influence on the crystalline and particle growth.[14]

Herein, we report an in-depth structural study of this class of materials by performing X-ray diffraction (XRD), X-ray absorption near-edge structure spectroscopy (XANES), and extended X-ray absorption fine structure spectroscopy (EXAFS) to further study the influence of the dopant on the crystallite structure and the effective incorporation of the dopant in the host lattice and to investigate the major differences between Co- and Fe-doped ZnO nanoparticles regarding the dopant oxidation state and the presence of local defects such as cationic vacancies or anionic interstitials caused by the substitution. X-ray absorption spectroscopy (XAS) is particularly suitable to obtain this information and has been largely used to investigate ZnO doped with transition metals (see ref 18 and references therein). Although other methods can, in principle, be used to derive the dopant oxidation state, here we used XAS because, besides providing oxidation states of the photoabsorbers with high accuracy, it can be also applied for future in situ studies of the same materials in-operando conditions.

EXPERIMENTAL SECTION

Synthesis of ZnO and TM-Doped ZnO. Zinc oxide as well as transition metal-doped zinc oxide was synthesized by dissolving the appropriate gluconate precursors (zinc(II) gluconate hydrate (ABCR), cobalt(II) gluconate hydrate (ABCR), iron(II) gluconate dihyrate (Aldrich)) in ultrapure water (Millipore). The total metal ion concentration was 0.2 M. The ratio between zinc and the transition metal ion was 9:1. This solution was then slowly added to a 1.2 M solution of sucrose (Acros Organics) and ultrapure water. After stirring at room temperature for about 15 min the water was evaporated at 160 °C. Subsequently, the temperature was increased to 300 °C in order to further dry the solution and start the decomposition of sucrose. To obtain pure oxides, the samples were calcined under air for 3 h at 450 °C for the iron-doped sample and at 400 °C for the cobalt-doped sample. The heating rate was set to 3 °C min^{-1}.

Carbon Coating of $Zn_{0.9}Fe_{0.1}O$. Carbon-coated Fe-doped zinc oxide was obtained by dispersing the as-prepared $Zn_{0.9}Fe_{0.1}O$ in an aqueous solution of sucrose, followed by an annealing step under inert gas atmosphere. In a first step, the dispersion of $Zn_{0.9}Fe_{0.1}O$ and sucrose in a weight ratio of 1:1 was homogenized by means of a planetary ball mill (Vario-Planetary Mill Pulverisette 4, Fritsch, milling time: 2 steps of 45 min with 10 min rest in between). The suspension was then dried at 80 °C under ambient atmosphere. After grinding, the resulting composite powder was annealed in a tubular furnace (R50/250/12, Nabertherm) at 500 °C for 4 h under a constant argon gas stream of about 750 mL min^{-1}. The heating rate was set to 3 °C min^{-1}. Finally, the thus-obtained powder was manually ground again. The carbon content of the composite material of about 20% was determined by means of thermogravimetric analysis (TGA, TA Instruments Q5000).

Powder XRD Characterization and Structural Refinement. The crystal structure of the as-synthesized samples was characterized by powder XRD with an automated Philips Bragg−Brentano diffractometer equipped with a graphite monochromator. The long fine-focus Cu tube was operated at 40 kV and 25 mA. Spectra were recorded in the 2θ range 15−140° with a 0.02° step and 9 s counting time. The structures were refined with the program GSAS.[19] The reflection shape was modeled with a pseudo-Voigt function; the full width at half-maximum (FWHM) was refined as a function of 2θ taking into account both Gaussian and Lorentzian broadening. The refinement was carried out in the space group $P6_3mc$, and the starting atomic coordinates were those of Xu and Ching[20] with the initial value for isotropic temperature factors (U_{iso}) arbitrarily chosen as 0.025 Å^2. The O atom sites were designated fully occupied, while constraints for fractional occupancies for Fe, Zn, and Co were used according to the stoichiometry of the synthesized samples. The background was modeled with 9- to 12-term polynomial functions. Cell parameters, scale factor, and the background polynomial function were free variables during the refinement. Parameters were added to the refinement in the following order: 2θ zero-shift, peak shape, peak asymmetry, atomic coordinates, and isotropic thermal factor. The intensity cutoff for the calculation of the profile step intensity was initially set at 1.0% of the peak maximum and, in the final stages of the refinement, was lowered to 0.1% of the peak maximum. Final convergence was considered reached when the parameter shifts were <1% of their respective estimated standard deviation. Estimated errors provided by the Rietveld refinement program are ±0.0002 Å for the cell parameters and ±0.002 Å for the selected interatomic distances. However, the error calculation is probably overoptimistic, as it does not include the correlation among parameters and other source of errors (like the overlapping of many diffraction reflections). In order to get an alternative estimate of the accuracy of the refined structural data, we have compared the set of structural parameters obtained using different refinement strategies on the same diffraction data. These comparisons show that realistic estimates of the error bars are ±0.0005 Å for the cell parameters and ±0.005 Å for the selected interatomic distances. The error in the estimation of phase content is ±1 wt %.

Using anisotropic thermal parameters led to an appreciable lowering of all the disagreement indexes. However, the unit cell parameters and individual interatomic distances were not affected by using isotropic vs anisotropic U. The shape of the oxygen thermal displacement factor ellipsoids displays a marked elongation parallel to the c axis. Here, we show the results obtained using isotropic temperature factors in the refinement procedure.

XAS Data Collection and Analysis. Samples for the XAS studies were prepared by pressing a homogeneous mixture of finely ground sample powder and cellulose powder into pellets. The amount of sample in each pellet was chosen to give an absorption $\mu_t \approx 1.5$, just above the selected absorption edge. XAS spectra at the Fe, Co, and Zn K-edges (7112, 7709, and 9659 eV, respectively) were collected at the GILDA-BM08 beamline[21] of the European Synchrotron Radiation Facility (ESRF, Grenoble, France). The storage ring was operated at 6 GeV in 16-bunch mode with a maximum electron current of 90 mA. The white beam delivered by the bending magnet source was monochromatized by using a fixed-exit double-crystal Si(311) monochromator operated in flat crystal mode. Two Pd-coated mirrors working at an incidence angle of 3.6 mrad were used for harmonics rejection. The second mirror was left unbent. In this configuration, the beam size at the sample was about 2 mm × 2 mm FWHM. XAS spectra were measured in transmission mode using two ionization chambers (I_0 and I_1) filled with N_2 and Ar gases at different pressures to achieve the optimal efficiency in the working energy range (20% and 80% of absorption, respectively). XAS spectra were measured at room temperature up to 1000 eV above the edge with a constant energy step of 0.2 eV in the XANES region, energy steps increasing from 1 to 4 eV in the EXAFS region, and an integration time of 4 s/point. The evaluated noise level was on the order of 2×10^{-4} for all the measured spectra. For each sample two spectra were averaged (four in the case of the Fe K-edge) in order to improve the signal-to-noise ratio.

XAS spectra of Fe, Co, and Zn metal foils placed in a second experimental chamber after the sample were acquired simultaneously with each sample scan for continuous monitoring of the energy scale against possible monochromator instabilities. No drifts of the energy scale were observed during the experiments. The edge energy was taken as the first maximum of the first derivative of the spectra. XAS measurements were also collected for a full set of compounds used as standards for the different Co and Fe oxidation states and coordination.

Fe K-edge pre-edge peak analysis was carried out following the same procedure reported in the references.[22−24] The pre-edge peak was fitted by a sum of pseudo-Voigt functions, and their intensities along with energy positions were compared with those of the standards analyzed here and others from the literature in order to extract information on the absorber oxidation state and coordination number in the synthesized samples. Particular care was taken in using the smallest possible number of components in the pre-edge peak fitting procedure. In particular, the number of components was constrained to be equal to the number of minima in the second derivative spectrum of the pre-edge peak. More details on the pre-edge peak fitting method can be found in refs 24 and 25. The Co K-edge XANES spectrum of $Zn_{0.9}Co_{0.1}O$ was compared with spectra of some Co model compounds containing solely octahedrally coordinated Co(II) [CoO], tetrahedrally coordinated Co(II) [$CoAl_2O_4$], and octahedrally coordinated Co(III) [$Co(C_5H_7O_2)_3$].[26]

■ RESULTS AND DISCUSSION

Powder XRD Characterization and Structural Refinement. The X-ray diffraction patterns of the synthesized samples are shown in Figure 1. All the diffraction reflections can be indexed according to the hexagonal ZnO structure ($P6_3mc$ space group). The patterns show sharp reflections indicating the formation of crystalline ZnO. A closer visualization of the patterns reveals the absence of reflections related to the presence of other phases (e.g., $ZnFe_2O_4$ or other iron oxides). Patterns collected with the same instrument on a mixture of ZnO and 0.5 wt % hematite (Fe_2O_3) showed obvious reflections corresponding to Fe_2O_3 (Figure S1, Supporting Information). Thus, we conclude that crystalline Fe-bearing impurities, if any, occur well below the 0.5 wt % level. Moreover, in the XRD pattern of $Zn_{0.9}Fe_{0.1}O/C$, no reflections corresponding to graphitic carbon are observed, indicating that the comprised carbon is amorphous. An increase of the FWHM of the diffraction reflections is evident (from bottom to top), revealing that different dopants and synthesis conditions remarkably affect the ZnO crystallinity.

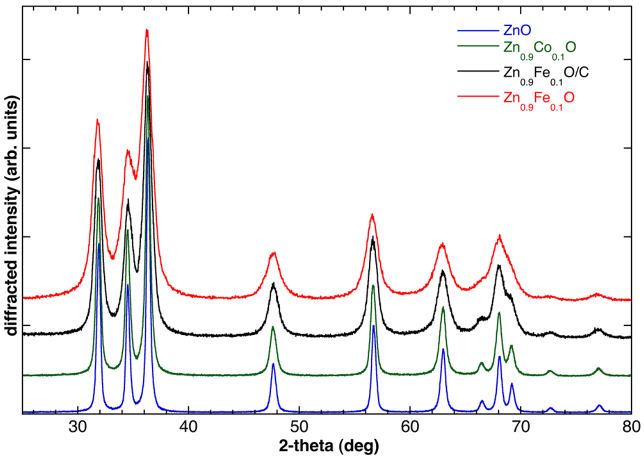

Figure 1. Experimental powder X-ray diffraction patterns: the change in line width associated with different doping or synthesis conditions is evident. Patterns were collected (and refined) in the range of 15° to 140°.

Rietveld refinement provided an accurate determination of the unit cell parameters and atomic positions. Table 1 summarizes the disagreement indexes, the most relevant structural parameters, and the average crystallite size (calculated using the Williamson–Hall method[27]). In Figure 2, a typical comparison between observed and calculated XRD patterns is displayed.

Table 1. Disagreement Indexes of the Rietveld Refinements Performed Using Isotropic Temperature Factors and Isotropic Broadening of the Diffraction Reflections

	ZnO	$Zn_{0.9}Co_{0.1}O$	$Zn_{0.9}Fe_{0.1}O$	$Zn_{0.9}Fe_{0.1}O/C$
a_0 (Å)	3.2511(3)	3.2523(1)	3.2552(2)	3.2547(1)
c_0 (Å)	5.2098(1)	5.2095(1)	5.2043(4)	5.2045(2)
V_0 (Å^3)	47.687(1)	47.721(1)	47.760(5)	47.746(2)
Zn–O (1×)	2.017	2.026	2.040	2.027
Zn–O (3×)	1.967	1.965	1.962	1.965
wRp	8.36	8.48	7.60	8.20
Rp	6.60	6.66	5.87	6.52
wRp − Bckg	7.75	8.14	7.41	7.80
RpBckg	6.28	6.46	5.75	6.34
R_{F^2}	3.49	3.69	4.19	4.09
R_F	1.92	1.87	2.30	2.22
c_0/a_0	1.6025	1.6018	1.5988	1.5990
W–H intercept[a]	0.0033	0.0048	0.011	0.0095
W–H slope[a]	0.0003	0.0006	0.0031	0.0009
crystallite size (nm)	42	29	13	15

[a] Fitted intercepts and slope of Williamson–Hall plots obtained using the refined peak shape parameters. The strain % is equal to the slope times 100.

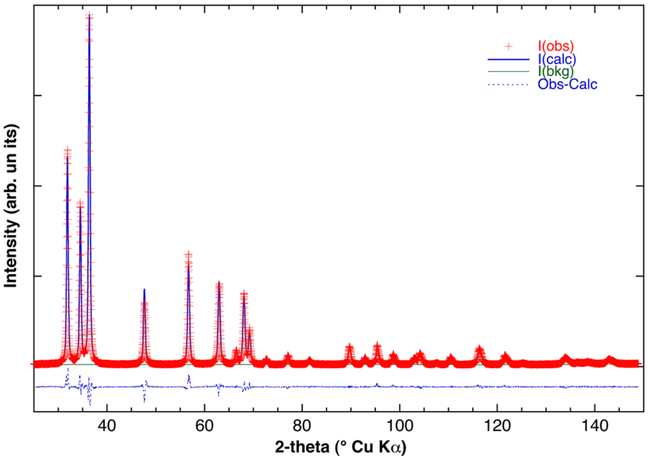

Figure 2. Example of Rietveld refinement of the ZnO sample: red crosses mark experimental data, the solid blue line and the green line represent the theoretical pattern and background function, respectively, and the dotted blue line is the residual.

The absence of any relevant amounts of Co- and Fe-bearing impurities in the XRD patterns of the doped samples suggests that Co and Fe were successfully introduced as dopants into the ZnO lattice.

The substitution of Zn by 0.1 atom per formula unit (apfu) of Co or Fe results in a small but appreciable variation of the unit cell volume. Although the variations are very small, the excellent agreement indexes of the fit (and the resulting small estimated errors of the unit cell parameters) allow the determination of these variations. The two iron-doped samples, with/without added carbon coating and accordingly with/without applying an additional heat treatment, display small variations of the unit cell parameter but within the estimated error. The variation of the unit cell size induced by the dopant provides further evidence for the successful incorporation of the transition metal into the ZnO lattice.

The FWHM of the XRD reflections increases in the order ZnO < $Zn_{0.9}Co_{0.1}O$ < $Zn_{0.9}Fe_{0.1}O/C$ < $Zn_{0.9}Fe_{0.1}O$, meaning that the crystallinity of the synthesis products decreases in the

DOI: 10.1021/acs.inorgchem.5b00493
Inorg. Chem. 2015, 54, 9393−9400

same order. The reflection shape parameters obtained from the Rietveld refinement were used to determine the diffraction reflection FWHM as a function of 2θ (Figure S2, Supporting Information) and to build Williamson−Hall (W−H) plots. The crystallite sizes, calculated by means of the Scherrer formula on the intercepts of the W−H plots, decrease from 42 nm to 13 nm in the sequence ZnO > $Zn_{0.9}Co_{0.1}O$ > $Zn_{0.9}Fe_{0.1}O/C$ > $Zn_{0.9}Fe_{0.1}O$, whereas the strain increases in the same order from 0.03% to 0.3%. In the absence of a calibration of the instrumental parameters of the utilized diffractometer, these values have to be taken as indicative and should not be considered as an absolute measure of the crystallite sizes. However, we note that these values are compatible with transmission electron microscopy (TEM) data reported for the same samples.[14] These results indicate that both doping and synthesis conditions can remarkably affect both the crystallinity and the strain of the studied samples.

The crystalline structure of ZnO consists of hexagonal close packing of oxygen anions with half of the available tetrahedral interstices occupied by Zn; this results in corner-sharing ZnO_4 tetrahedra with a face orthogonal to the *c* crystallographic axis and an apical oxygen directed along the *c* crystallographic direction. In order to test if part of the dopants could have entered interstitial sites, further refinements have been performed forcing partial occupations of the interstitial octahedral or tetrahedral sites, sharing a face with the Zn tetrahedra (respectively Wyckoff notation 2b at 1/3,2/3,−0.2258 and Wyckoff notation 2a at 0,0,0.1321). Even for very small Fe or Co occupancies of interstitial sites (0.005 apfu) all the disagreement indexes (e.g., R_F or R_{F^2}) increased reproducibly with respect to those obtained assuming no dopant in the interstitial sites (from 10% to >100% increase, assuming 0.005 to 0.05 apfu occupancy of the interstitial sites by the dopants). This test further confirmed that the dopants substitute Zn and are virtually absent in the interstitial sites.

It is worth remarking that the cell parameters' variations are not related solely to the ionic radii of the substituting cations (0.60, 0.49, and 0.58 Å for tetrahedrally coordinated Zn^{2+}, Fe^{3+}, and Co^{2+} according to ref 28). In fact, besides displaying compositional variations, the samples studied here also show different crystallinity and, possibly, the presence of defects such as cationic vacancies and/or interstitial oxygen (see following paragraphs). Both crystallinity and the presence of defects strongly contribute to alter unit cell parameters[29] in a not simply predictable way.

XANES and Pre-edge Peak Analysis. Normalized XANES spectra collected at the Zn, Co, and Fe K-edges are presented in Figures 3 and 4. All spectra collected at the Zn K-edge display similar features compared to those of undoped ZnO reported in the literature.[30] No significant changes are noticed in terms of peak energy position and relative intensity between spectra of samples containing different dopants, testifying that the dopant, at this concentration, does not greatly affect the local environment of Zn.

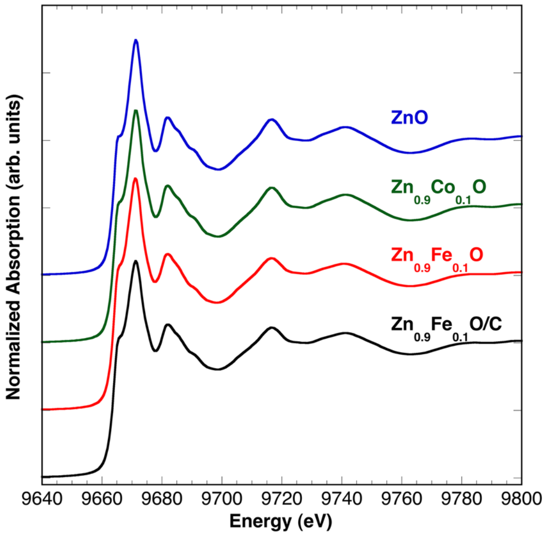

Figure 3. Normalized XANES spectra collected at the Zn K-edge. The curves were vertically offset for clarity.

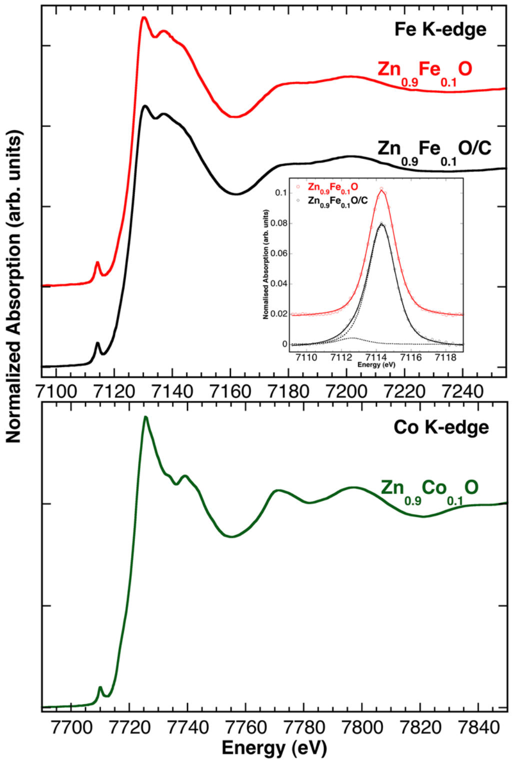

Figure 4. Normalized XANES spectra collected at the Fe (upper panel) and Co K-edge (lower panel). Curves in the upper panel were vertically offset for clarity.

The Co K-edge (Figure 4, lower panel) spectrum compares well with those already reported for Co-doped ZnO.[31,32] Both the edge energy and the pre-edge peak energy and intensity are compatible with those of tetrahedrally coordinated Co^{2+} model compounds (see Figure S3, Supporting Information), suggesting that Co substitutes Zn in the tetrahedral site of the ZnO lattice (isovalent substitution). From the XANES region there is no evidence for the presence of metallic Co clusters. In previous studies, the "valley" between the pre-edge peak and the onset of absorption was found to fill with an increasing metallic fraction.[32,33] Here, there is a clear gap and the evaluated ratio between the height and the depth of the pre-edge feature is 1.83(1), therefore ruling out the formation of metallic nanoclusters, according to the criterion established in ref 32.

The Fe K-edge XANES spectra obtained for $Zn_{0.9}Fe_{0.1}O$ and $Zn_{0.9}Fe_{0.1}O/C$ (Figure 4, upper panel) display similar features. Nevertheless, a small shift to lower energies of the edge for the sample $Zn_{0.9}Fe_{0.1}O/C$ compared to $Zn_{0.9}Fe_{0.1}O$ (7126.9 and 7127.5 eV, respectively) suggests a small variation of the Fe

Table 2. Pseudo-Voigt Parameters of the Components Used for the Pre-edge Peak Fit for $Zn_{0.9}Fe_{0.1}O$ and $Zn_{0.9}Fe_{0.1}O/C$

	energy (eV)	intensity	FWHM (eV)	% Lorentzian character	total area	centroid (eV)
$Zn_{0.9}Fe_{0.1}O$	7114.32	0.084	1.820	52.51	0.172	7114.32
$Zn_{0.9}Fe_{0.1}O/C$						
1st pV	7112.63	0.004	1.874	59.43	0.010	
2nd pV	7114.32	0.082	1.874	59.43	0.170	
weighted sum pV					0.180	7114.23

oxidation state (possibly iron is more reduced in the sample synthesized with carbon).

The background-subtracted pre-edge peaks (Figure 4, inset of the upper panel) are also similar regarding their shape and intensity. However, while the pre-edge peak of $Zn_{0.9}Fe_{0.1}O$ can be fitted with only one pseudo-Voigt component at 7114.32 eV (typical of Fe^{3+}), the spectrum of $Zn_{0.9}Fe_{0.1}O/C$ can be fitted also with an additional component at 7112.63 eV, compatible with the presence of a small fraction of Fe^{2+}. Attempts to fit also the spectrum of $Zn_{0.9}Fe_{0.1}O$ with two components always failed (resulting in negative intensities of the component at 7112.63 eV).

These data imply that, within error, Fe in $Zn_{0.9}Fe_{0.1}O$ can be regarded as purely trivalent, whereas in $Zn_{0.9}Fe_{0.1}O/C$ a small contribution from Fe^{2+} can be assumed. To estimate the amount of divalent iron present in $Zn_{0.9}Fe_{0.1}O/C$, we compared the pre-edge peak integrated intensities and energy centroids (Table 2) with those of model compounds from the literature (Figure S4, Supporting Information). The resulting $Fe^{3+}/(Fe^{2+} + Fe^{3+})$ ratios are 1.0 ± 0.05 for $Zn_{0.9}Fe_{0.1}O$ and 0.95 ± 0.05 for $Zn_{0.9}Fe_{0.1}O/C$. The integrated intensity of the two samples is typical of Fe model compounds with an average coordination number of five. Fe^{3+} model compounds in tetrahedral coordination so far reported in the literature (e.g., refs 22−25 and references therein) display integrated intensities ranging from 0.4 down to 0.25. The lower intensity of the two Fe-doped ZnO samples may be explained either by the presence of Fe in two different sites [one tetrahedral (substituting Zn) and one interstitial octahedral site] or by the unexpected lowering of the pre-edge peak intensity, possibly due to the geometrical distortion of the tetrahedra occupied by Fe and the presence of an oxygen atom that, despite being at a longer distance (ca. 3.2 Å instead of 1.98 Å), is centrosymmetrically oriented with respect to the apical oxygen of the Fe-centered tetrahedron. Given the ascertained absence of significant amounts of Fe in interstitial sites of the ZnO lattice and the absence of crystalline impurities in the studied samples, we attribute the unexpectedly lower intensity of the pre-edge peak to the geometrical configuration of the Fe sites (i.e., comparatively longer Fe−O distances with respect to other known FeO_4 tetrahedra[25]) or, alternatively, to the possible presence of interstitial oxygen atoms close to Fe sites.

EXAFS Results. The k-weighted EXAFS signals $k^2\chi(k)$, measured at the Fe, Co, and Zn K-edges, are presented in Figure 5. The $k^2\chi(k)$ signals were Fourier transformed with a Kaiser−Bessel window in the 2−12 $Å^{-1}$ k-range. The moduli of the Fourier transforms (FT) are shown in Figure 6 (dots). In pure ZnO, Zn is coordinated with four oxygen atoms at about 1.98 Å in a slightly distorted tetrahedron. The next nearest coordination shell is formed by 12 Zn atoms (six at 3.21 Å and six at 3.25 Å). The FT shown in Figure 6 presents two strong peaks corresponding to the first- and next-neighbor coordination shells, respectively. The peak positions are shifted to lower distances with respect to the actual interatomic distances since no phase shift corrections were applied.

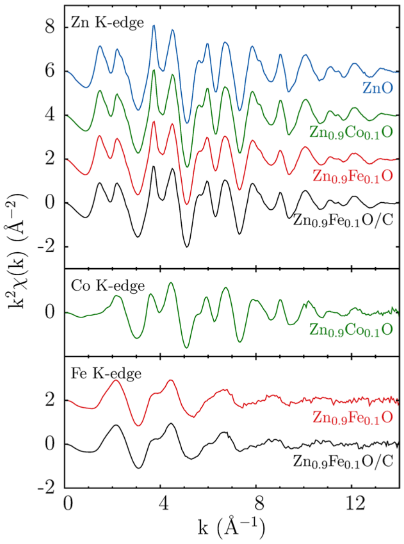

Figure 5. k-weighted EXAFS signals $k^2\chi(k)$ measured at the Zn K-edge (top panel), Co K-edge (middle panel), and Fe K-edge (bottom panel) for the full set of investigated samples. The curves in each panel are vertically shifted for clarity reasons.

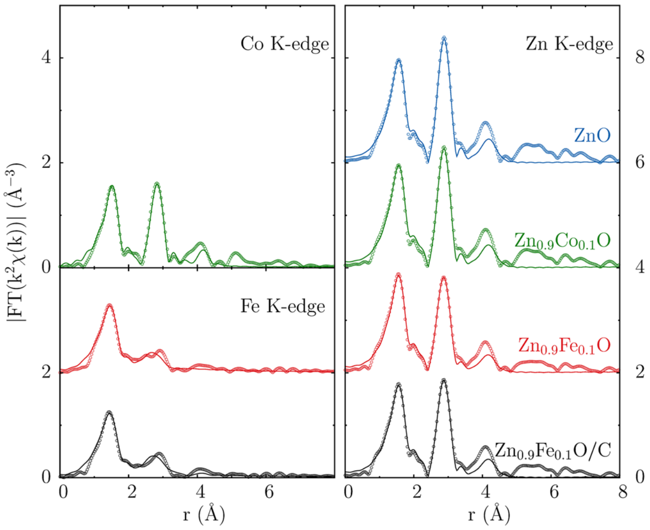

Figure 6. Magnitude of the Fourier-transformed EXAFS signals $k^2\chi(k)$ (dots) measured at the Co K-edge (top left panel), Fe K-edge (bottom left panel), and Zn K-edge (right panel) for all investigated samples. The best fit curves are also shown (solid lines). Curves in each panel are vertically shifted for clarity reasons.

The experimental EXAFS signals at the Zn K-edge (Figure 5, top panel) show similar features, the most notable differences residing in the intensity of the peak related to the second coordination shell in the FT spectra (Figure 6, right panel), which slightly decreases in the order ZnO, $Zn_{0.9}Co_{0.1}O$, $Zn_{0.9}Fe_{0.1}O/C$, and $Zn_{0.9}Fe_{0.1}O$.

The experimental EXAFS signal measured at the Co K-edge (Figure 5, middle panel) shows features similar to those of the Zn K-edge. This provides further qualitative evidence that Co fully substitutes for Zn in the tetrahedral sites of the host lattice and there are no other Co phases or metallic Co present in interstitial sites, in agreement with previous reports on Co-doped ZnO thin films,[34,35] nanowires,[36] and nanopowders.[37] In previous EXAFS studies of transition metal-doped ZnO,[33,38−40] even a few percent fraction of metallic clusters or impurities in the oxide phases were clearly identified in the EXAFS signal. In particular, the peak associated with the first shell of the metal was clearly visible in the FT between the first and second shell peaks characteristic of ZnO.

The experimental EXAFS signals at the Fe K-edge of both $Zn_{0.9}Fe_{0.1}O$ and $Zn_{0.9}Fe_{0.1}O/C$ (Figure 5, lower panel) show the same features albeit with strongly damped amplitudes compared to those at Zn and Co K-edges. This suggests a modification of the Fe local environment from the one of the Zn and Co sites. In particular, the intensity of the peak related to the second coordination shell in the FT modulus displays a marked decrease compared to the spectra taken at the Zn and Co K-edges, implying strong modifications of the distribution or number of Zn atoms in the second coordination shell. The existence of metallic clusters can be excluded because there are no detectable contributions from Fe metal in the FT.

To obtain quantitative structural information, the EXAFS signals were analyzed by means of the IFEFFIT package.[41] Theoretical backscattering amplitudes and phase shifts were calculated via the FEFF8.1 code[42] using a self-consistent energy-dependent exchange correlation Hedin−Lundqvist potential. For ZnO, theoretical signals were calculated for the wurtzite structure obtained from XRD. For Fe- and Co-doped ZnO, the clusters around the Fe or Co photoabsorbers where built from the same structure by locating them in the same ZnO structure. Since Fe (or Co) and Zn backscattering amplitudes are fairly similar, the backscatters were always assumed to be Zn.

Fits were performed in the R-space in the interval 1−3.4 Å and all the coordination shells up to such cutoff distance were included in the theoretical model. The coordination numbers were kept fixed to those of crystalline ZnO. The mean value of the interatomic distance and their variance (σ^2) relative to the first Zn(Co,Fe)-O shell were left as free parameters. A single isotropic expansion/contraction of the average distance was allowed for each signal pertinent to the successive coordination shells. Figure 6 also shows the comparison of the experimental FT of the EXAFS signal (dots) and the best fit curves (solid lines). The main results are summarized in Tables S2 and S3 (Supporting Information). The presence of Co and Fe metallic clusters or an additional amorphous γ-Fe_2O_3 phase was carefully examined and finally ruled out.

Results of the fits performed at the Zn K-edge reveal that the local environment of Zn atoms is almost not affected by the presence of Fe/Co dopants, in agreement with previous reports.[39] Nonetheless, the variance σ^2 of the Zn−Zn(Fe/Co) distance distribution slightly increases in $Zn_{0.9}Fe_{0.1}O/C$ and $Zn_{0.9}Fe_{0.1}O$, possibly indicating a higher level of structural disorder of the second coordination shell in Fe-doped samples.

As far as the Co K-edge is concerned, the fit demonstrates that Co substitutes Zn within the ZnO wurtzite structure. The first neighbor Co−O distance is comparable to those reported in the literature[36] and is slightly shorter than that found for undoped ZnO, as expected considering the effective ionic radii of Zn^{2+} (0.60 Å) and Co^{2+} (0.58 Å) in tetrahedral coordination.[28]

From the fit of the EXAFS signals measured at the Fe K-edge in $Zn_{0.9}Fe_{0.1}O$ and $Zn_{0.9}Fe_{0.1}O/C$ we gain deeper insight into the modifications of the wurtzite crystalline lattice around Fe^{3+} ions. The first-shell signal is well reproduced by assuming that Fe substitutes Zn in tetrahedral sites. The first-shell Fe−O distances are significantly shorter (∼1.8%) than for ZnO and Co-doped ZnO, consistently with the reduced ionic radius of Fe^{3+} in tetrahedral coordination (0.49 Å). The Debye−Waller factor (σ^2) of the Fe−Zn bonds is very large (and its determination is affected by a larger error), as the FT peak corresponding to the second coordination shell is weaker compared to the signals measured at the Co and Zn edges. In general, the Debye−Waller factors (σ^2) for all the shells are larger than the values obtained for Co-doped ZnO.

The increased disorder in both the first and second shell is attributed to the occurrence of local defects in the immediate environment of Fe^{3+} in tetrahedral sites, in agreement with both the results of crystallinity as obtained by XRD and the Fe oxidation states as deduced by XANES. Indeed, the presence of Zn vacancies ($2Fe_{subs}$−Zn_{vac}) is compatible with the aliovalent substitution of Fe^{3+} for Zn^{2+}, since the presence of trivalent cations substituting divalent Zn implies the presence of Shottky defects. If 0.1 Fe^{3+} apfu is located in the tetrahedral sites normally occupied by Zn, then the charge conservation requires that 0.05 vacancy per formula unit exists in the tetrahedral sites. The strong reduction of the second-shell Fe−Zn(Fe) contribution to the EXAFS signal would imply a higher amount of vacancies compared to a simple $2Fe_{subs}$−Zn_{vac} mechanism. A possible explanation could be either an increased structural disorder around Fe, triggered by vacancies, or a scenario in which Fe ions (and consequently Zn vacancies) are clustered together around oxygen atoms in the ZnO lattice. Because of the similar atomic numbers between Fe and Zn scatters, the present data do not provide sufficient evidence to distinguish whether the substitutional Fe^{3+} ions are homogeneously distributed rather than clustered (i.e., forming FeO_4 dimers or oligomers) throughout the lattice.[36] Moreover, other charge compensating complexes could be also considered such as interstitial oxygen ($2Fe_{subs}$−O_{int}).[43] Further work involving XANES calculations and ab initio structural modeling is in progress in order to clarify this open issue.

CONCLUSIONS

The present XRD, XANES, and EXAFS investigation of Co- and Fe-doped ZnO reveal the effective incorporation of such transition metal dopants into the host materials without the formation of metallic nanoclusters or additional oxide phases. Both dopants Co and Fe are located in the tetrahedral sites of the ZnO lattice (Wyckoff notation 2b) substituting for Zn. No significant fractions of both Fe and Co were found in the interstitial sites in either tetrahedral or octahedral coordination. XANES data clearly reveal that Co is divalent, whereas Fe is mostly trivalent in the investigated samples. The presence of Fe^{3+} (substituting for Zn^{2+}) implies the existence of local defects in the structure (such as cationic vacancies or interstitial oxygen) for charge compensation. This hypothesis is supported by the EXAFS data: while at the Co K-edge there is a clear contribution to the EXAFS signal associated with the Co−Zn second coordination shell, for the Zn K-edge signals, the corresponding signal is strongly damped at the Fe K-edge. This intensity reduction may be attributed to the occurrence of local defects triggered by the presence of trivalent Fe^{3+} such as Zn vacancies or interstitial oxygen ions.

The herein presented results are of substantial importance to unfold the (de)lithiation mechanism in general as well as in dependence on the incorporated dopant. We propose that the different oxidation state of the Fe and Co dopant is reflected in the different shape of the recorded potential profiles of such materials,[14] indicating a slightly different (initial) lithiation reaction during cycling. In addition, we assume that the absence of metallic TM nanophases in the pristine material enables the excellent reversibility of the Li_2O formation during cycling. Synthesis of metal oxide solid solution with a controllable defect chemistry and defect concentration could be of fundamental importance in order to tailor the physical properties of ZnO material.[44] However, these considerations will have to be confirmed by in situ/in operando studies, for which the herein reported results serve as a base and starting point.

■ ASSOCIATED CONTENT

Ⓢ Supporting Information

The Supporting Information is available free of charge on the ACS Publications website at DOI: 10.1021/acs.inorgchem.5b00493.

> Analysis of the FWHM of the XRD peaks; Fe K-edge pre-edge peak analysis; Co K-edge XANES for $Zn_{0.9}Co_{0.1}O$ and three model compounds; tables with results of the EXAFS data analysis (PDF)

■ AUTHOR INFORMATION

Corresponding Author

*E-mail: gabriele.giuli@unicam.it.

Author Contributions

The manuscript was written through contributions of all authors. All authors have given approval to the final version of the manuscript.

Notes

The authors declare no competing financial interest.

■ ACKNOWLEDGMENTS

The authors F.M., D.B., and S.P. would like to thank BMW AG (ABILE project) for financial support.

■ REFERENCES

(1) Bruce, P. G.; Freunberger, S. A.; Hardwick, L. J.; Tarascon, J.-M. *Nat. Mater.* **2011**, *11*, 19−29.

(2) Bresser, D.; Passerini, S.; Scrosati, B. *Chem. Commun.* **2013**, *49*, 10545−10562.

(3) Larcher, D.; Beattie, S.; Morcrette, M.; Edström, K.; Jumas, J.-C.; Tarascon, J.-M. *J. Mater. Chem.* **2007**, *17*, 3759−3772.

(4) Poizot, P.; Laruelle, S.; Grugeon, S.; Dupont, L.; Tarascon, J.-M. *Nature* **2000**, *407*, 496−499.

(5) NuLi, Y.-N.; Chu, Y.-Q.; Qin, Q.-Z. *J. Electrochem. Soc.* **2004**, *151*, A1077−A1083.

(6) Sharma, Y.; Sharma, N.; Subba Rao, G. V.; Chowdari, B. V. R. *Adv. Funct. Mater.* **2007**, *17*, 2855−2861.

(7) Sharma, Y.; Sharma, N.; Rao, G. V. S.; Chowdari, B. V. R. *Electrochim. Acta* **2008**, *53*, 2380−2385.

(8) Guo, X.; Lu, X.; Fang, X.; Mao, Y.; Wang, Z.; Chen, L.; Xu, X.; Yang, H.; Liu, Y. *Electrochem. Commun.* **2010**, *12*, 847−850.

(9) Deng, Y.; Zhang, Q.; Tang, S.; Zhang, L.; Deng, S.; Shi, Z.; Chen, G. *Chem. Commun.* **2011**, *47*, 6828−6830.

(10) Ding, Y.; Yang, Y.; Shao, H. *Electrochim. Acta* **2011**, *56*, 9433−9438.

(11) Liu, B.; Zhang, J.; Wang, X.; Chen, G.; Chen, D.; Zhou, C.; Shen, G. *Nano Lett.* **2012**, *12*, 3005−3011.

(12) Bresser, D.; Paillard, E.; Kloepsch, R.; Krueger, S.; Fiedler, M.; Schmitz, R.; Baither, D.; Winter, M.; Passerini, S. *Adv. Energy Mater.* **2013**, *3*, 513−523.

(13) Mueller, F.; Bresser, D.; Paillard, E.; Winter, M.; Passerini, S. *J. Power Sources* **2013**, *236*, 87−94.

(14) Bresser, D.; Mueller, F.; Fiedler, M.; Krueger, S.; Kloepsch, R.; Baither, D.; Winter, M.; Paillard, E.; Passerini, S. *Chem. Mater.* **2013**, *25*, 4977−4985.

(15) Varzi, A.; Bresser, D.; von Zamory, J.; Müller, F.; Passerini, S. *Adv. Energy Mater.* **2014**, *4*, n/a.

(16) Dietl, T.; Ohno, H.; Matsukura, F.; Cibert, J.; Ferrand, D. *Science* **2000**, *287*, 1019−1022.

(17) Sato, K.; Katayama-Yoshida, H. *Phys. E* **2001**, *10*, 251−255.

(18) Mino, L.; Agostini, G.; Borfecchia, E.; Gianolio, D.; Piovano, A.; Gallo, E.; Lamberti, C. *J. Phys. D: Appl. Phys.* **2013**, *46*, 423001.

(19) Larson, A. C.; Von Dreele, R. B. *Gen. Struct. Anal. Syst. Rep. LAUR* **1998**, 86−748.

(20) Xu, Y.-N.; Ching, W. Y. *Phys. Rev. B: Condens. Matter Mater. Phys.* **1993**, *48*, 4335−4351.

(21) D'Acapito, F.; Trapananti, A.; Torrengo, S.; Mobilio, S. *Not. Neutroni E Luce Sincrotrone* **2014**, *19*, 14−23.

(22) Wilke, M.; Farges, F.; Petit, P.-E.; Brown, G. E.; Martin, F. *Am. Mineral.* **2001**, *86*, 714−730.

(23) Giuli, G.; Pratesi, G.; Cipriani, C.; Paris, E. *Geochim. Cosmochim. Acta* **2002**, *66*, 4347−4353.

(24) Giuli, G.; Pratesi, G.; Eeckhout, S. G.; Koeberl, C.; Paris, E. *Spec. Pap. - Geol. Soc. Am.* **2010**, *465*, 653−660.

(25) Giuli, G.; Cicconi, M. R.; Paris, E. *Eur. J. Mineral.* **2012**, *24*, 783−790.

(26) Maurizio, C.; El Habra, N.; Rossetto, G.; Merlini, M.; Cattaruzza, E.; Pandolfo, L.; Casarin, M. *Chem. Mater.* **2010**, *22*, 1933−1942.

(27) Mote, V. D.; Purushotham, Y.; Dole, B. N. *J. Theor. Appl. Phys.* **2012**, *6*, 6.

(28) Shannon, R. D. *Acta Crystallogr., Sect. A: Cryst. Phys., Diffr., Theor. Gen. Crystallogr.* **1976**, *32*, 751−767.

(29) Hazen, R. M.; Jeanloz, R. *Rev. Geophys.* **1984**, *22*, 37−46.

(30) Guglieri, C.; Céspedes, E.; Prieto, C.; Chaboy, J. *J. Phys.: Condens. Matter* **2011**, *23*, 206006.

(31) Shi, T.; Zhu, S.; Sun, Z.; Wei, S.; Liu, W. *Appl. Phys. Lett.* **2007**, *90*, 102108.

(32) Ney, A.; Opel, M.; Kaspar, T. C.; Ney, V.; Ye, S.; Ollefs, K.; Kammermeier, T.; Bauer, S.; Nielsen, K.-W.; Goennenwein, S. T. B.; Engelhard, M. H.; Zhou, S.; Potzger, K.; Simon, J.; Mader, W.; Heald, S. M.; Cezar, J. C.; Wilhelm, F.; Rogalev, A.; Gross, R.; Chambers, S. A. *New J. Phys.* **2010**, *12*, 013020.

(33) Heald, S. M.; Kaspar, T.; Droubay, T.; Shutthanandan, V.; Chambers, S.; Mokhtari, A.; Behan, A. J.; Blythe, H. J.; Neal, J. R.; Fox, A. M.; Gehring, G. A. *Phys. Rev. B: Condens. Matter Mater. Phys.* **2009**, *79*, 075202.

(34) Martínez-Criado, G.; Segura, A.; Sans, J. A.; Homs, A.; Pellicer-Porres, J.; Susini, J. *Appl. Phys. Lett.* **2006**, *89*, 061906.

(35) Sun, Z.; Yan, W.; Zhang, G.; Oyanagi, H.; Wu, Z.; Liu, Q.; Wu, W.; Shi, T.; Pan, Z.; Xu, P.; Wei, S. *Phys. Rev. B: Condens. Matter Mater. Phys.* **2008**, *77*, 245208.

(36) Yao, T.; Yan, W.; Sun, Z.; Pan, Z.; Xie, Y.; Jiang, Y.; Ye, J.; Hu, F.; Wei, S. *J. Phys. Chem. C* **2009**, *113*, 14114−14118.

(37) He, R.; Hocking, R. K.; Tsuzuki, T. *Mater. Chem. Phys.* **2012**, *132*, 1035−1040.

(38) Wei, H.; Yao, T.; Pan, Z.; Mai, C.; Sun, Z.; Wu, Z.; Hu, F.; Jiang, Y.; Yan, W. *J. Appl. Phys.* **2009**, *105*, 043903.

(39) Mino, L.; Gianolio, D.; Bardelli, F.; Prestipino, C.; Kumar, E. S.; Bellarmine, F.; Ramanjaneyulu, M.; Lamberti, C.; Rao, M. S. R. *J. Phys.: Condens. Matter* **2013**, *25*, 385402.

(40) Vachhani, P. S.; Dalba, G.; Ramamoorthy, R. K.; Rocca, F.; Šipr, O.; Bhatnagar, A. K. *J. Phys.: Condens. Matter* **2012**, *24*, 506001.

(41) Ravel, B.; Newville, M. *J. Synchrotron Radiat.* **2005**, *12*, 537–541.

(42) Ankudinov, A. L.; Rehr, J. J. *Phys. Rev. B: Condens. Matter Mater. Phys.* **2000**, *62*, 2437–2445.

(43) Xiao, J.; Kuc, A.; Pokhrel, S.; Schowalter, M.; Parlapalli, S.; Rosenauer, A.; Frauenheim, T.; Mädler, L.; Pettersson, L. G. M.; Heine, T. *Small* **2011**, *7*, 2879–2886.

(44) Li, G.; Smith, R. L.; Inomata, H. *J. Am. Chem. Soc.* **2001**, *123*, 11091–11092.